



Research Paper

Temperature dependent thermal transport in graphene paper above room temperature



Jianshu Gao^a, Chuizhou Meng^b, Danmei Xie^{a,*}, Chenyang Liu^c, Hua Bao^{c,*}, Bo Yang^d,
Maodong Li^d, Yanan Yue^{a,*}

^a Key Laboratory of Hydraulic Machinery Transients (MOE), School of Power and Mechanical Engineering, Wuhan University, Wuhan, Hubei 430072, China

^b Hebei Key Laboratory of Smart Sensing and Human-Robot Interaction, School of Mechanical Engineering, Hebei University of Technology, Tianjin 300401, China

^c University of Michigan-Shanghai Jiao Tong University Joint Institute, Shanghai Jiao Tong University, Shanghai 200240, China

^d National Graphene Center (Guangdong), Guangzhou Special Pressure Equipment Inspection and Research Institute, Guangzhou 510663, China

HIGHLIGHTS

- Thermal conductivity of graphene paper is highly temperature dependent.
- The temperature-dependent property is attributed to the morphology and inner-structural change.
- Graphene paper exhibits much better cooling performance than conventional cooling films.

ARTICLE INFO

Keywords:

Graphene paper
Thermal conductivity
Temperature dependence
Thermal management

ABSTRACT

Graphene paper (GP) is more feasible to be integrated as a heat spreader than monolayer graphene due to its controllable size and moderate reduction in thermal transport properties. In this work, we fabricated and characterized GP to understand its thermal transport properties based on thermal bridge method combined with transient electro-thermal technique. The thermal conductivity of GP exhibits a highly temperature dependent property from 637 W/mK at room temperature to 757 W/mK at 80 °C, which is contrary to the trend of monolayer graphene. The increasing thermal property can be partially ascribed to the morphological and inner-structural change of the composite at elevated temperatures. Surface roughness is found to be reduced by 30% from atomic force microscope imaging. This feature is beneficial for many industrial applications such as the cooling film in smartphones. The implementation of GP is further verified in a smartphone to simulate the heat-dissipation performance. The results show that GP with temperature dependent properties exhibits much better cooling performance than conventional cooling films such as copper film.

1. Introduction

High intrinsic thermal conductivity of monolayer graphene and its great potential in thermal management have attracted much attention [1]. The extremely small thickness and size impede the real applications unless the bulk material with high thermal conductivity becomes possible [2–4]. A proper integration of graphene laminate in plastic materials [5] as thermal interface materials can significantly improve the heat-dissipation performance [6–9]. However, for free-standing graphene, the increase in layer number [10], residue impurities, defects and disorder [11] would contribute to large reduction in thermal properties [12]. The integration of graphene into bulk structures while retaining the excellent thermal/mechanical properties is a challenge.

Advance in material science has made it possible to fabricate large-scale GP with only moderate damage to its two-dimensional structure [13,14]. Compared with the commercial thermal conductor such as copper thin film with thermal conductivity of ~400 W/mK [15], GP might be promising in thermal management applications [16].

Many efforts have been devoted to obtaining high thermal conductivity of GP. For example, Kong et al. prepared a flexible graphene-carbon fiber composite film by depositing the graphene oxide (GO) into carbon fiber precursor followed by carbonization [17]. The graphene was partly separated by a 3D carbon fiber framework to reduce the phonon leakage at interface. Thermal conductivity of their sample was reported to be 977 W/mK. Shen et al. obtained the graphitizing GO film by directly evaporating the GO suspension under mild heating [18].

* Corresponding authors.

E-mail addresses: dmxie@whu.edu.cn (D. Xie), hua.bao@sjtu.edu.cn (H. Bao), yyue@whu.edu.cn (Y. Yue).

<https://doi.org/10.1016/j.applthermaleng.2019.01.098>

Received 14 November 2018; Received in revised form 24 January 2019; Accepted 28 January 2019

Available online 29 January 2019

1359-4311/ © 2019 Elsevier Ltd. All rights reserved.

They claimed that the interface thermal resistance and phonon-boundary scattering were suppressed and a high thermal conductivity was obtained: 1100 W/mK. In order to control the alignment and thickness of graphene inside the GP, Xin et al. employed the direct electro-spray deposition method to increase the thermal conductivity [19]. Their results revealed that thermal conductivity of GP is sensitive to the treatment temperature and average size of graphene flakes.

It has been reported that the treatment temperature in synthesis process could change the structure and then thermal properties, while the operating temperature also affects the heat transfer performance, especially for most carbon materials [20,21]. The temperature dependent thermal conductivity of carbon-based structures including carbon nanotube (CNT), graphene and diamond can be described by Umklapp phonon scattering theory [22,23]. This value increases firstly toward transition temperature (usually less than 300 K) and then decreases in a $1/T$ relation for a large temperature range [24,25]. However, for carbon-based composites, temperature dependent properties are more complicated when both phonon-boundary and phonon-defect scatterings are all involved [26,27]. For example, thermal conductivity of CNT fiber is enhanced by two folds (from 40 to 105 W/mK) within a temperature increasing from 93 °C to 253 °C [28]. As a highly porous structure, thermal conductivity of graphene foam is much lower and is also sensitive to temperature (from 0.3 W/mK at 27 °C to 1.5 W/mK at 177 °C) [29]. Considering that the GP in this work consists of graphene flakes under the van der Waals interaction, the phonon-boundary scattering at the interface could change the thermal properties as temperature increases.

Thermal characterization works of different GPs have been reported based on different techniques (listed in Table 1). The large variation in the reported values stems from (1) differences in the quality of GP since they are prepared with different methods, and (2) differences in characterization methods that might introduce uncertainties if not carefully controlled in the measurement. The large diversity of reported values is not surprising [30,31]. In this work, we fabricate a GP by graphitizing the GO film, and characterize its thermophysical properties based on a thermal bridge method, and then combine with the transient electro-thermal technique to investigate the comprehensive thermal properties of GP. Most importantly, we study the temperature dependent thermophysical properties and validate the great potential for applications in thermal management.

2. Measurement principle and experimental details

2.1. Synthesis and structural characterization of GP

Our GP is synthesized from the GO film which is prepared by the modified Hummer's method. It is dispersed into the solution with a concentration of 10 mg/mL. The GO slurry is uniformly attached to a polyethylene terephthalate (PET) film among an open-air environment

Table 1
Reported values of thermal conductivity of GP.

	Materials	Measurement Methods	k(W/mK)
Peng et al. [16]	GP	Laser flash	1940
Kong et al. [17]	Graphene-carbon fiber paper	Laser flash	977
Shen et al. [18]	GP	Laser flash	1100
Xin et al. [19]	GP	Laser flash	~1434
Hou et al. [48]	GP	Modified laser heating angstrom	220–390
Kumar et al. [30]	Reduced GO paper	Laser flash	1390
Xie et al. [61]	GP	Transient electro-thermal	634–710 at RT
Ding et al. [74]	GP	Laser flash	1842
Our work	GP	Thermal bridge	637

to evaporate the water inside the sample. In order to remove the oxygen-containing functional groups and the possible organic impurities, the individual GO film separated from PET is immersed in a carbonization environment of 1100–1300 °C for 30 min. Furthermore, the film is highly graphitized at around 2800 °C for 1 h and then slowly cooled down to room temperature with argon gas protection during the whole process. Wrinkled structure of graphene flakes appears inside the porous graphene film and then expands along the cross-plane direction. Two smooth stainless flakes are used to press the film under a high pressure of 100 MPa for 1 h. Finally, a GP with a dense structure is obtained.

Fig. 1(a) presents a scanning electron microscope (SEM) image of GP sample in cross-section direction. It is found that the graphene flakes closely stack with each other along the cross-section direction. The layer-by-layer nanostructure determines a dense assembly. Two parallel lines were introduced in the inset as a comparison to demonstrate the uniform thickness of GP (37.3 μm). The small wrinkles at GP surface are shown in Fig. 1(b). The GP exhibits excellent flexibility, as shown in the inset of Fig. 1(b). It can be bent, rolled or even folded without any cracking. The emission and reflection spectra of GP characterized by Fourier transform infrared spectroscopy (FTIR) are shown in Fig. 1(c). According to the radiation relation of $\varepsilon = \int_0^\infty [1 - \rho(\lambda) - \tau(\lambda)] E_{b\lambda} d\lambda / E_b$ [32], where $\rho(\lambda)$ is the spectral reflectivity, $\tau(\lambda)$ is the spectral transmissivity, $E_{b\lambda}$ is the spectral emissive power, E_b is the blackbody emission, the overall emissivity of GP is obtained as 0.3345, which is much smaller than that of natural graphite [33]. Wang et al. indicated that the emissivity is sensitive to the surface microstructure of graphite [34]. The wrinkled nanostructures upon the surface of GP affect the emissivity significantly, which could be the main reason for the discrepancy between GP and graphite material.

As the Raman spectrum with a wavelength of 532 nm in laser excitation shown in Fig. 1(d), the inconspicuous D peak (1350 cm^{-1}) indicates a low defect level and good crystalline structure inside GP [35]. The intensity ratio of D peak to G peak (I_D/I_G) is sensitive to the crystallite size of graphene under a certain wavelength of Raman laser [36]. In Fig. 1(d), the I_D/I_G is determined as 0.0186, indicating a crystallite size of $1.03 \mu\text{m}$ [37,38], which is 11 times larger than that of raw graphite [39]. The inset shows an asymmetric structure of the 2D signal. Lorentz function is applied to fit 2D peak into two peaks (G'_{3DA} peak and G'_{3DB} peak). Since the 2D peak is sensitive to the structure of graphene, the stacking order of graphene flakes inside GP is in AB Bernal [40] and similar to that of highly oriented pyrolytic graphite [41]. The layer number of graphene flakes can be identified from the intensity ratio of 2D peak to G peak. Raman spectra are collected from four positions for averaging. The ratio is determined to be 0.19–0.20, demonstrating that there are five or more layers of graphene in GP sample [42]. Previous study shows that thermal conductivity of graphene with a layer number larger than 5 at room temperature is comparable to that of graphite [43].

2.2. Thermal conductivity measurement

The schematic of the thermal-bridge method for thermal conductivity (k) measurement is shown in Fig. 2. The sample is suspended between a heater and a heat sink inside a vacuum chamber. The heating current is supplied and carefully controlled by a DC current source. Heat is transferred from the heater to the heat sink through GP. Thermal equilibrium can be established between the Joule heating and the thermal transport through heat conduction and thermal radiation. According to Fourier's law, k can be described as

$$k = \frac{qL}{Wd(T_1 - T_2)} \quad (1)$$

where L , W , d , T_1 , T_2 , q are the sample length, width, thickness, heater temperature, heat sink temperature, heat conduction, respectively. Among these parameters, the q can be described as $q = IU$

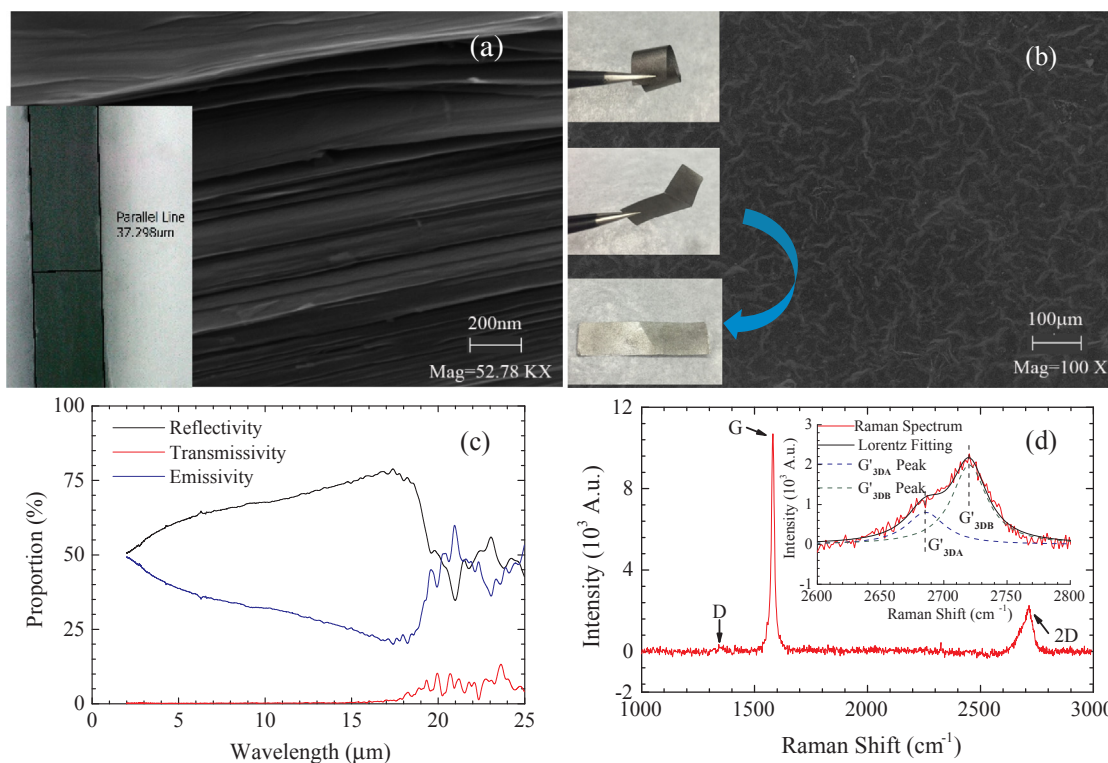


Fig. 1. SEM image of GP (a) in cross-section direction with a thickness of 37.3 μm shown in inset and (b) in-plane direction. The insets show excellent flexibility of samples. (c) The emission, reflection and transmission spectra of GP. (d) The Raman spectrum of GP.

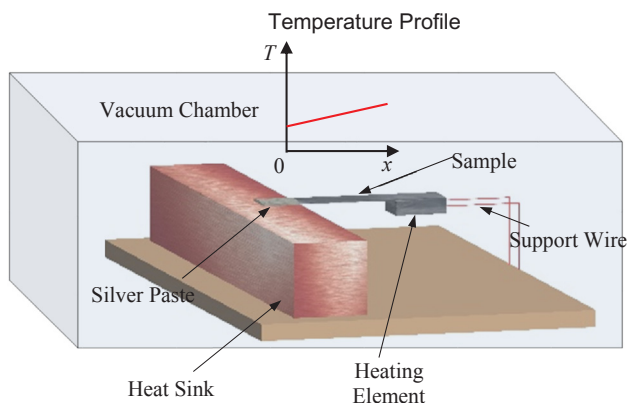


Fig. 2. The schematic of thermal-bridge method for thermal conductivity measurement.

$\epsilon S_1 \sigma (T_1^4 - T_0^4) - \epsilon S_2 \sigma (T_a^4 - T_0^4)$, where I , U , ϵ , S_1 , S_2 , σ , T_a are constant current, voltage, emissivity of GP (obtained as 0.3345 from measurement), surface area of heater, surface area of GP, Stephen-Boltzmann constant, average temperature of GP, respectively.

Three samples are obtained from the same piece of GP with dimensions of $5.00 \times 10.82 \text{ mm}^2$, $5.00 \times 15.18 \text{ mm}^2$ and $5.00 \times 18.64 \text{ mm}^2$, respectively. The thickness of GP is $37.3 \mu\text{m}$ as mentioned above. The heater has the same width as GP to ensure a perfect fit and silver paste is used to connect the sample and the heater to reduce thermal contact resistance. The measuring stage is placed in a vacuum chamber under 1mTorr to eliminate heat convection effect. Various currents from 100 mA to 400 mA are applied to the heater. Temperature is monitored by a thermocouple when a steady state along the sample is established. Each measurement is repeated several times for averaging to reduce measurement uncertainty.

3. Results and discussions

3.1. Temperature dependent thermal conductivity

Compared with laser-based techniques, the thermal bridge method features simple setup and straight-forward measurement strategy. The heating density can be precisely controlled, which involves less uncertainties. The k results of three GP samples are shown in Fig. 3. Similar trends of k with respect to temperature are found for all samples. The k at room temperature is characterized as 637 W/mK. Compared to the results in opening literatures in Table 1, the variation is reasonable considering the discrepancy in sample preparation and the measuring methods. The k of GP is much lower than that of monolayer graphene

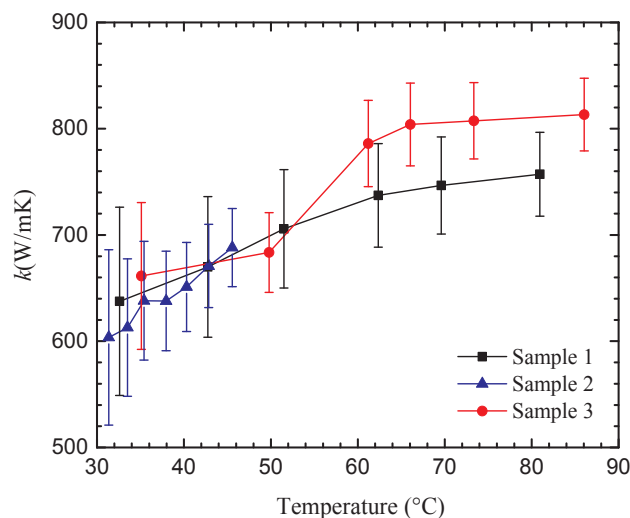


Fig. 3. Characterization results of temperature dependent thermal conductivity of GP.

[44], which is also reasonable considering the thickness of samples. The k is decreased dramatically with the increase of atomic layer due to the enhancement of phase-space states in phonon dispersion [23]. Furthermore, the presence of large numbers of contact interfaces for graphene flakes inside GP introduces intense phonon scattering in thermal transport.

It is found that the k of GP is increased from 637 W/mK to 757 W/mK as the temperature is increased from room temperature to 81 °C, which is aligned well with the operating temperatures for most electronics. According to Umklapp theory, the k of graphene at above room temperature decreases with respect to temperature [45]. The transition temperature is usually below 300 K [46]. For GP samples, even though the high temperature treatment in graphitization process introduces a defect repairing process [47], there still exist some deficiencies inside GP due to the observation of D peak in Fig. 1d [48]. The phonon-boundary scattering and phonon-defect scattering are all involved in the thermal transport process. Temperature rise might introduce a structural modification and thus affect the phonon scattering and the overall thermal properties. The GP consisting of graphene flakes and other composites evolves a certain thermal expansion during heating process. k is more sensitive to interface mismatch between graphene flakes and adjacent mater other than the Umklapp phonon scattering [49].

3.2. Morphological change at elevated temperatures

To confirm this, we used the atomic force microscope (AFM) to study the morphological change of GP at elevated temperatures. As shown in Fig. 1(b), there exists many small wrinkled nanostructures at the GP surface, which could lead to strong phonon scattering and could be the main reason for reduced k [50–52]. The k can be reduced by wrinkled nanostructures by introducing a compressive strain [53]. Fig. 4(a) presents the surface morphology of GP at different temperatures: the height distribution curve along the red line is shown as an

inset. The arithmetical mean deviation of assessed profile (R_a) is introduced to study the surface morphological change during the heating process, and is calculated as [54]

$$R_a = \frac{\sum_{i=1}^N |y_i - \bar{y}|}{N} \quad (2)$$

where $|y_i - \bar{y}|$ is the absolute variation between the roughness profile and the mean line. The GP sample is heated by a heating platform beneath it. In Fig. 4(b), it is demonstrated that R_a is decreased from 2.86 nm to 2.01 nm with temperature from 25 °C to 80 °C for the same position. As illustrated in Fig. 4(c), temperature rise introduces a tensile strain to the wrinkled nanostructures, resulting in a decrease in surface roughness [55]. Among the temperature range of 25–80 °C, the Umklapp phonon scattering contributes to a decreasing k by 24% for monolayer graphene and 10% for graphite, respectively [46]. Since five or more layers of graphene in GP sample has been demonstrated in Raman measurement, the decrease of k introduced by Umklapp phonon scattering is within the range of 10–24%. However, a reduction of 30% in surface roughness changes the overall phonon transport properties in GP. The phonon-boundary scattering at wrinkled nanostructure is suppressed significantly, especially for those surfaces that are smoother. As a combined effect, the k of GP increases over the measured temperature range [56]. Chen et al. measured the k of suspended graphene with and without wrinkled nanostructure by micro-Raman mapping [57]. The k of graphene without wrinkled nanostructure is about 27% higher than that with wrinkled nanostructures. Wang et al. calculated the anisotropic k of graphene with wrinkled nanostructures [58]. k could be reduced by 80% for wrinkled nanostructures compared with the initial graphene.

3.3. Characterization of thermal diffusivity and capacity

In order to systematically investigate the thermal transport properties, thermal diffusivity of our GP is characterized by the transient

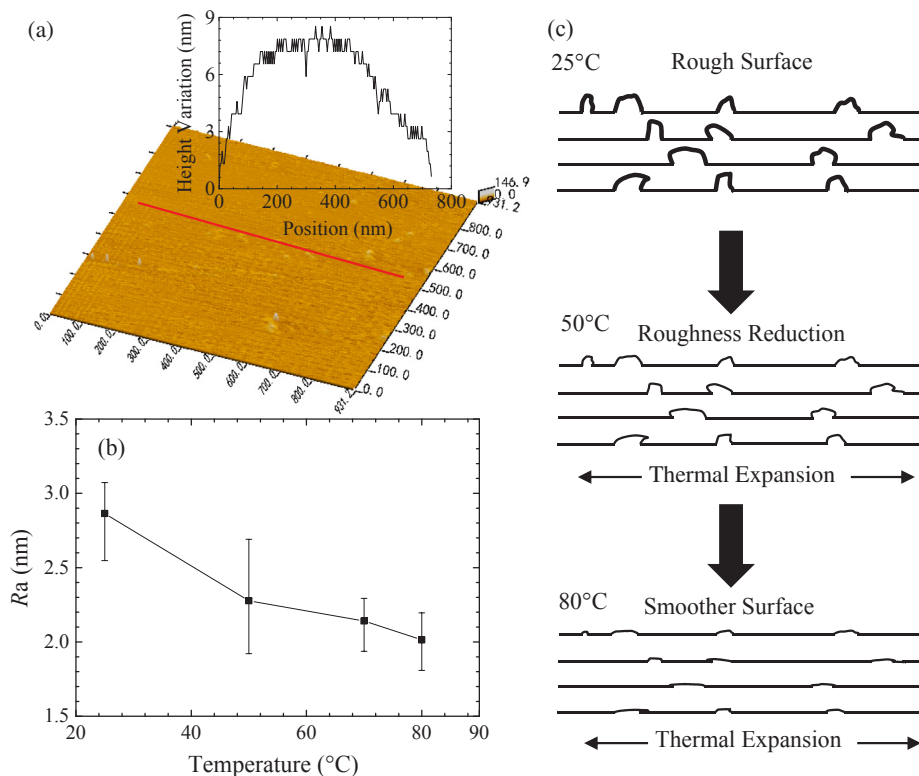


Fig. 4. (a) AFM image of the GP surface at temperature of 80 °C. The inset presents the height variation along the red line. (b) The variation of R_a with respect to temperature. (c) The schematic of morphological change induced by thermal expansion.

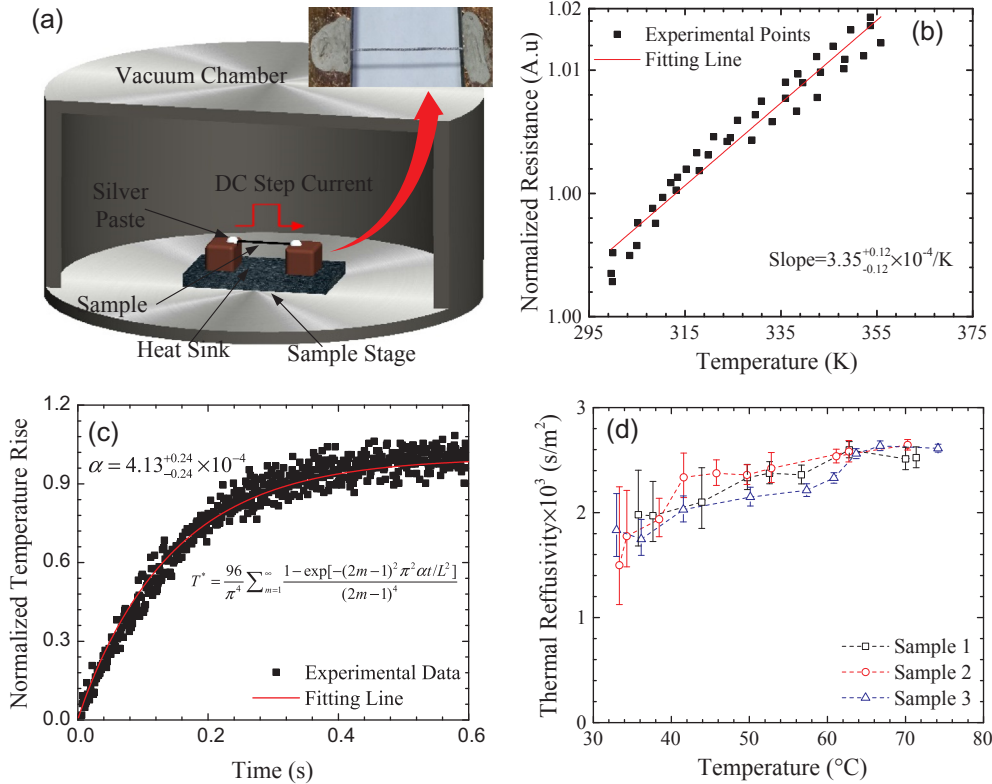


Fig. 5. (a) The schematic of TET technique for thermal diffusivity measurement. (b) The linear relationship between normalized resistance and temperature for GP. (c) Normalized temperature rise during heating process. (d) Thermal reffusivity with respect to temperature.

electro-thermal (TET) technique [59,60]. Three GP samples are prepared from the same original piece with lengths of 14.86 mm, 17.60 mm and 23.38 mm, respectively. As shown in Fig. 5(a), the sample is suspended between two copper electrodes with silver paste to ensure a good electrical and thermal contact in the vacuum chamber. A DC step current from 90 mA to 210 mA is applied to the sample to introduce Joule heating. The normalized temperature rise can be determined as

$$T^* = \frac{96}{\pi^4} \sum_{m=1}^{\infty} \frac{1 - \exp[-(2m-1)^2 \pi^2 \alpha t / L^2]}{(2m-1)^4} \quad (3)$$

where α is thermal diffusivity, L is sample length, t is heating time. The sample temperature is sensitive to electrical resistance. Therefore, the normalized temperature rise can be obtained from the voltage evolution, and is described as $[U(t)-U_0]/(U_1-U_0)$, where $U(t)$, U_0 and U_1 is the voltage at time t , initial and final voltages over the sample, respectively.

Fig. 5(b) shows the linear relationship between resistance and temperature over a temperature range of 25–85 °C. A fitting line is established to determine a linear relationship with a normalized temperature coefficient of $3.35^{+0.12}_{-0.12} \times 10^{-4}/K$. The experimentally normalized temperature rise during heating process is presented in Fig. 5(c). The α of GP is fitted among $3.78 \times 10^{-4} \text{ m}^2/\text{s}$ – $5.63 \times 10^{-4} \text{ m}^2/\text{s}$ under different heating currents with 95% confidence interval. Xie and Wang et al. determined a α of GP as $6.15 \times 10^{-4} \text{ m}^2/\text{s}$ at room temperature from the increasing behavior of normalized voltage variation during heating process [61]. The values are also consistent well with the measured results from other group [17]. In addition, thermal reffusivity (Θ , inverse α) can be used to study the phonon thermal resistivity in GP [62]. It is found that Θ varies slightly from $2 \times 10^3 \text{ s/m}^2$ to $2.5 \times 10^3 \text{ s/m}^2$ in the measured temperature range as shown in Fig. 5(d). Considering the single relaxation time approximation, Θ is determined to be $\Theta = 3/(\nu^2 \tau)$ [63], where ν is the phonon velocity, and is insensitive to temperature. τ is the relaxation time for phonon scattering. According

to the Matthiessen’s rule, τ is determined by the Umklapp, defect and boundary phonon scattering. The phonon relaxation time of Umklapp increases exponentially with temperature. Phonon relaxation time induced by defect and boundary is determined by the internal structure of GP. Since the morphology is changed during the heating process as demonstrated by AFM imaging. The τ is sensitive not only to the Umklapp phonon scattering, but also to the defect and boundary phonon scattering induced by the change of internal structure during temperature rise [64], and thus contributes to a combined mode in Fig. 5(d).

The specific heat capacity (C_p) is estimated from the measurement results of α and k : $C_p = k/\alpha\rho$, where ρ is the density of GP and is calculated from the sample mass and geometry at room temperature [65]. Four samples in different dimension are tested and the density is determined as $952.16^{+88.33}_{-88.33} \text{ kg/m}^3$. The uncertainty is from standard deviation among measurement results. Considering that k and α values at room temperature, the C_p of our sample is estimated as $1184^{+121}_{-106} \text{ J/(kg}\cdot\text{K)}$. Literatures have shown that the ρ and C_p for bulk graphite materials at room temperature is measured to be 2250 kg/m^3 [66] and $709 \text{ J/(kg}\cdot\text{K)}$ [25], respectively. Although our GP undergoes a high compression process to integrate the porous structure into a dense film, the assembly between different graphene layers is much weaker than bulk graphite materials, which indicates a smaller density for GP. The wrinkled nanostructures introduce a residual strain in GP, and could influence C_p significantly [67,68]. The existence of wrinkled nanostructures in GP could be responsible for the difference of C_p between GP and bulk graphite materials.

3.4. Heat dissipation inside a smartphone by numerical simulations

The temperature dependent thermal properties of our GP sample are very attractive for industrial applications such as smartphone and laptop. In order to determine the performance, three-dimensional steady numerical simulations are implemented in ANSYS software. The

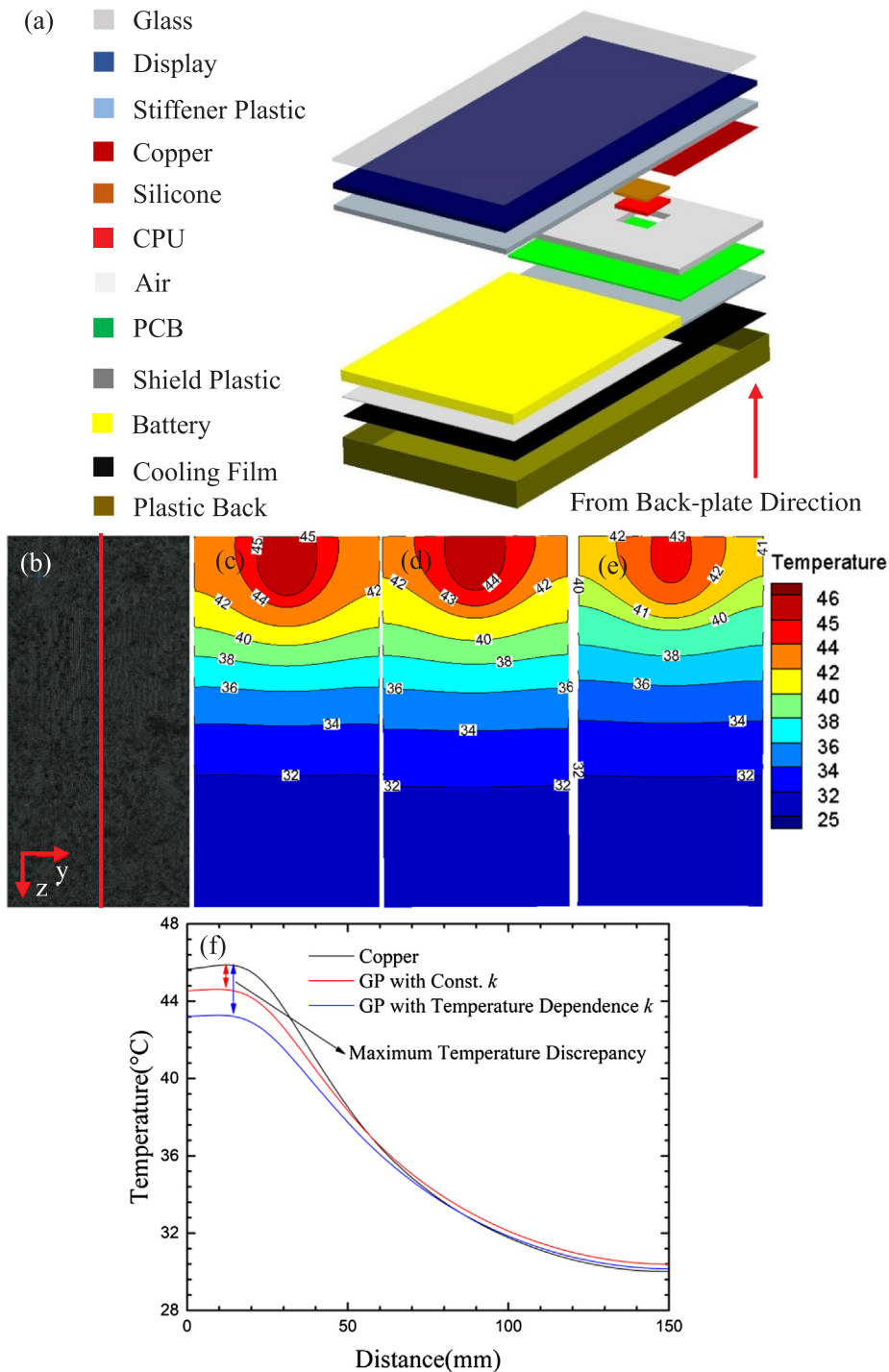


Fig. 6. (a) The schematic components of a smartphone. (b) A finite element model of a cooling film. Temperature distribution of cooling films in (c) copper, (d) GP with constant k and (e) GP with temperature dependent k , respectively. (f) Temperature profile along the red line in (b) for different cooling films.

cooling film was applied between the plastic shield and the back plate within the phone. The schematic of internal structure of a typical smartphone is shown in Fig. 6(a). Thermal properties of different components used in the simulation are listed in Table 2 [69–72]. The cooling film is switched to different materials including copper, GP film with constant thermal properties and a GP film with temperature dependent k . The CPU acts as a heater with a constant operating power of 2.5 W. The convective heat transfer coefficient at the phone surface is $5 \text{ W/m}^2\text{K}$ and emissivity is 0.92 for the environment temperature of 25°C [73]. The heat generated by the CPU dissipates to the surroundings to the phone surface. The total number of nodes and elements are

modeled as 2,385,689 and 573,517, respectively. To verify the grid independence of the simulations, the node number has been varied between 645,759 and 3,615,264. It is found that the obtained results exhibits an independent trend when the node number is at above 2,385,689. In all simulations, the governing partial differential equations per unit volume were solved with an iterative convergence of 10^{-4} .

Fig. 6(c–e) shows the simulation results. It is found that the heat-dissipation performance of GP film is better than that of copper film as shown in Fig. 6(c) and (d) in terms of lower temperature values and a more uniform temperature distribution. When considering the

Table 2
Material properties used in simulation.

Materials	Thickness (mm)	k (W/mK)
Glass	1.0	1.0
Display Lumped	2.0	$k_{yz} = 1.8$, $k_x = 0.1$
Plastic	–	0.1
Copper	37.3 μm	401
GP with constant k	37.3 μm	$k_{yz} = 637$, $k_x = 10$
GP with temperature dependent k	37.3 μm	k_{yz} is presented as experimental result of sample 1 in Fig. 3, $k_x = 10$
Silicone	1.0	2.0
CPU	1.4	150
Air	–	0.0263
PCB	0.8	$k_{yz} = 45$, $k_x = 1.0$
Battery	4.0	$k_{yz} = 15$, $k_x = 1.0$

temperature dependent thermal properties, the maximum temperature of GP film (in Fig. 6e) is even lower. Temperature profiles along the red line in Fig. 6(b) for three cases are summarized in Fig. 6(f). The maximum temperature drops between GP (with constant properties) and copper is 1.33 °C (red¹ arrow). This value reaches 2.64 °C (blue arrow) when considering temperature dependent properties. The results demonstrate that the temperature dependent thermal property of GP is very promising for heat dissipation.

4. Conclusions

In summary, we synthesized a large-area GP sample and characterized its thermophysical properties over the range of possible operating temperature. The k of GP at 80 °C is 18.76% larger than that at room temperature due to the morphological and inner-structure change during the temperature rise. The surface roughness is decreased by 30% as determined from AFM imaging, indicating a smoother nanostructures of GP at higher temperatures. The cooling performance of GP inside a smartphone is simulated, and the results show that the use of GP (especially considering the temperature dependent properties) is much better than using a conventional copper film. Our finding in this work can promote the applications of GP in thermal management.

Acknowledgments

The financial support from the National Natural Science Foundation of China (Nos. 51576145, 51676121, 51776142) is gratefully acknowledged.

Appendix A. Supplementary material

Supplementary data to this article can be found online at <https://doi.org/10.1016/j.applthermaleng.2019.01.098>.

References

- [1] D.J. Renteria, L.D. Nika, A.A. Balandin, Graphene thermal properties: applications in thermal management and energy storage, *Appl. Sci.* 4 (2014).
- [2] R. Prasher, Graphene spreads the heat, *Science* 328 (2010) 185–186.
- [3] Y. Yue, J. Zhang, Y. Xie, W. Chen, X. Wang, Energy coupling across low-dimensional contact interfaces at the atomic scale, *Int. J. Heat Mass Transf.* 110 (2017) 827–844.
- [4] Y. Yue, J. Zhang, X. Tang, S. Xu, X. Wang, Thermal transport across atomic-layer material interfaces, *Nanotechnol. Rev.* 4 (2015) 533–555.
- [5] H. Malekpour, K.H. Chang, J.C. Chen, C.Y. Lu, D.L. Nika, K.S. Novoselov, A.A. Balandin, Thermal conductivity of graphene laminate, *Nano Lett.* 14 (2014) 5155–5161.
- [6] M. Saadah, E. Hernandez, A. Balandin, Thermal management of concentrated multi-junction solar cells with graphene-enhanced thermal interface materials, *Appl. Sci.* 7 (2017) 589.
- [7] F. Kargar, Z. Barani, M. Balinskiy, A.S. Magana, J.S. Lewis, A.A. Balandin, Dual-functional graphene composites for electromagnetic shielding and thermal management, *Adv. Electron. Mater.* (2018) 1800558.
- [8] F. Kargar, Z. Barani, R. Salgado, B. Debnath, J.S. Lewis, E. Ayta, R.K. Lake, A.A. Balandin, Thermal percolation threshold and thermal properties of composites with high loading of graphene and boron nitride fillers, *ACS Appl. Mater. Inter.* 10 (2018) 37555–37565.
- [9] W. Yu, C. Liu, L. Qiu, P. Zhang, W. Ma, Y. Yue, H. Xie, L.S. Larkin, Advanced thermal interface materials for thermal management, *Eng. Sci.* 2 (2018) 95–97.
- [10] L.N. Denis, A.B. Alexander, Phonons and thermal transport in graphene and graphene-based materials, *Rep. Prog. Phys.* 80 (2017) 036502.
- [11] J.D. Renteria, S. Ramirez, H. Malekpour, B. Alonso, A. Centeno, A. Zurutuza, A.I. Cocemasov, D.L. Nika, A.A. Balandin, Strongly anisotropic thermal conductivity of free-standing reduced graphene oxide films annealed at high temperature, *Adv. Funct. Mater.* 25 (2015) 4664–4672.
- [12] W. Zhao, W. Chen, Y. Yue, S. Wu, In-situ two-step Raman thermometry for thermal characterization of monolayer graphene interface material, *Appl. Therm. Eng.* 113 (2017) 481–489.
- [13] H. Wu, L. Drzal, Graphene nanoplatelet paper as a light-weight composite with excellent electrical and thermal conductivity and good gas barrier properties, *Carbon* 50 (2012) 1135–1145.
- [14] X. Ye, Q. Zhou, C. Jia, Z. Tang, Y. Zhu, Z. Wan, Producing large-area, foldable graphene paper from graphite oxide suspensions by in-situ chemical reduction process, *Carbon* 114 (2017) 424–434.
- [15] D. Liu, P. Chen, H. Huang, Realization of a thermal cloak-concentrator using a metamaterial transformer, *Sci. Rep.* 8 (2018) 2493–2493.
- [16] L. Peng, Z. Xu, Z. Liu, Y. Guo, P. Li, C. Gao, Ultrahigh thermal conductive yet superflexible graphene films, *Adv. Mater.* 29 (2017).
- [17] Q.Q. Kong, Z. Liu, J.G. Gao, C.M. Chen, Q. Zhang, G. Zhou, Z.C. Tao, X.H. Zhang, M.Z. Wang, F. Li, Hierarchical graphene-carbon fiber composite paper as a flexible lateral heat spreader, *Adv. Funct. Mater.* 24 (2014) 4222–4228.
- [18] B. Shen, W. Zhai, W. Zheng, Ultrathin flexible graphene film: an excellent thermal conducting material with efficient EMI shielding, *Adv. Funct. Mater.* 24 (2014) 4542–4548.
- [19] G. Xin, H. Sun, T. Hu, H.R. Fard, X. Sun, N. Koratkar, T. Borca-Tasciuc, J. Lian, Large-area freestanding graphene paper for superior thermal management, *Adv. Mater.* 26 (2014) 4521–4526.
- [20] J. Liu, W. Qu, Y. Xie, B. Zhu, T. Wang, X. Bai, X. Wang, Thermal conductivity and annealing effect on structure of lignin-based microscale carbon fibers, *Carbon* 121 (2017) 35–47.
- [21] H. Lin, H. Dong, S. Xu, X. Wang, J. Zhang, Y. Wang, Thermal transport in graphene fiber fabricated by wet-spinning method, *Mater. Lett.* 183 (2016) 147–150.
- [22] A.A. Balandin, D.L. Nika, Phononics in low-dimensional materials, *Mater. Today* 15 (2012) 266–275.
- [23] A.A. Balandin, Thermal properties of graphene and nanostructured carbon materials, *Nat. Mater.* 10 (2011) 569–581.
- [24] A. Cepellotti, G. Fugallo, L. Paulatto, M. Lazzeri, F. Mauri, N. Marzari, Phonon hydrodynamics in two-dimensional materials, *Nat. Commun.* 6 (2015) 6400.
- [25] E. Pop, V. Varshney, A.K. Roy, Thermal properties of graphene: fundamentals and applications, *MRS Bull.* 37 (2012) 1273–1281.
- [26] A.M. DíezPascual, J. Guan, B. Simard, M.A. GómezFatou, Poly(phenylene sulphide) and poly(ether ether ketone) composites reinforced with single-walled carbon nanotube buckypaper: II – Mechanical properties, electrical and thermal conductivity, *Compos. Part A-App. S.* 43 (2012) 1007–1015.
- [27] M. Li, C. Li, J. Wang, X. Xiao, Y. Yue, Parallel measurement of conductive and convective thermal transport of micro/nanowires based on Raman mapping, *Appl. Phys. Lett.* 106 (2015) 253108.
- [28] Y. Yue, K. Liu, M. Li, X. Hu, Thermal manipulation of carbon nanotube fiber by mechanical stretching, *Carbon* 77 (2014) 973–979.
- [29] M. Li, Y. Sun, H. Xiao, X. Hu, Y. Yue, High temperature dependence of thermal transport in graphene foam, *Nanotechnology* 26 (2015) 105703.
- [30] P. Kumar, F. Shahzad, S. Yu, S.M. Hong, Y.H. Kim, C.M. Koo, Large-area reduced graphene oxide thin film with excellent thermal conductivity and electromagnetic interference shielding effectiveness, *Carbon* 94 (2015) 494–500.
- [31] M. Akoshima, K. Hata, D. Futaba, K. Mizuno, T. Baba, M. Yumura, Thermal diffusivity of single-walled carbon nanotube forest measured by laser flash method, *Jpn. J. Appl. Phys.* 48 (2009) 05EC07.
- [32] H. Bao, C. Yan, B. Wang, X. Fang, C.Y. Zhao, X. Ruan, Double-layer nanoparticle-based coatings for efficient terrestrial radiative cooling, *Sol. Energy Mat. Sol. C* 168 (2017) 78–84.
- [33] A.G. Ageev, D.I. Kavyrshin, M.A. Sargsyan, M.K. Gadzhiev, V.F. Chinnov, Determination of graphite sublimation rate in high enthalpy plasma flow using ‘laser knife’ method, *Int. J. Heat Mass Transf.* 107 (2017) 146–153.
- [34] F. Wang, L. Cheng, H. Mei, Q. Zhang, L. Zhang, Effect of surface microstructures on the infrared emissivity of graphite, *Int. J. Thermophys.* 35 (2014) 62–75.
- [35] A. Eckmann, A. Felten, A. Mischenko, L. Britnell, R. Krupke, K.S. Novoselov, C. Casiraghi, Probing the nature of defects in graphene by Raman spectroscopy, *Nano Lett.* 12 (2012) 3925–3930.
- [36] A.C. Ferrari, D.M. Basko, Raman spectroscopy as a versatile tool for studying the properties of graphene, *Nat. Nanotechnol.* 8 (2013) 235–246.
- [37] Y. Zhang, T. Liu, B. Meng, X. Li, G. Liang, X. Hu, Q.J. Wang, Broadband high photoresponse from pure monolayer graphene photodetector, *Nat. Commun.* 4 (2013) 1811.
- [38] T. Deng, X. Zhou, Porous graphite prepared by molybdenum oxide catalyzed

¹ For interpretation of color in Fig. 6, the reader is referred to the web version of this article.

- gasification as anode material for lithium ion batteries, *Mater. Lett.* 176 (2016) 151–154.
- [39] L. Kou, H. He, C. Gao, Click chemistry approach to functionalize two-dimensional macromolecules of graphene oxide nanosheets, *Nano-Micro Lett.* 2 (2010) 177–183.
- [40] L. Malard, M. Pimenta, G. Dresselhaus, M. Dresselhaus, Raman spectroscopy in graphene, *Phys. Rep.* 473 (2009) 51–87.
- [41] M. Pimenta, G. Dresselhaus, M.S. Dresselhaus, L. Cancado, A. Jorio, R. Saito, Studying disorder in graphite-based systems by Raman spectroscopy, *Phys. Chem. Chem. Phys.* 9 (2007) 1276–1290.
- [42] I. Calizo, I. Bejenari, M. Rahman, G. Liu, A.A. Balandin, Ultraviolet Raman microscopy of single and multilayer graphene, *J. Appl. Phys.* 106 (2009) 043509.
- [43] Z. Wang, R. Xie, C.T. Bui, D. Liu, X. Ni, B. Li, J.T.L. Thong, Thermal transport in suspended and supported few-layer graphene, *Nano Lett.* 11 (2011) 113–118.
- [44] S. Ghosh, W. Bao, D.L. Nika, S. Subrina, E.P. Pokatilov, C.N. Lau, A.A. Balandin, Dimensional crossover of thermal transport in few-layer graphene, *Nat. Mater.* 9 (2010) 555.
- [45] H. Wang, S. Hu, K. Takahashi, X. Zhang, H. Takamatsu, J. Chen, Experimental study of thermal rectification in suspended monolayer graphene, *Nat. Commun.* 8 (2017) 15843.
- [46] G. Fugallo, A. Cepellotti, L. Paulatto, M. Lazzeri, N. Marzari, F. Mauri, Thermal conductivity of graphene and graphite: collective excitations and mean free paths, *Nano Lett.* 14 (2014) 6109–6114.
- [47] J. Chen, T. Shi, T. Cai, T. Xu, L. Sun, X. Wu, D. Yu, Self healing of defected graphene, *Appl. Phys. Lett.* 102 (2013) 103107.
- [48] Z.L. Hou, W.L. Song, P. Wang, M.J. Meziani, C.Y. Kong, A. Anderson, H. Maimaiti, G.E. LeCroy, H. Qian, Y.P. Sun, Flexible graphene-graphene composites of superior thermal and electrical transport properties, *ACS Appl. Mater. Inter.* 6 (2014) 15026–15032.
- [49] Y. Xie, S. Xu, Z. Xu, H. Wu, C. Deng, X. Wang, Interface-mediated extremely low thermal conductivity of graphene aerogel, *Carbon* 98 (2016) 381–390.
- [50] Y. Kuang, L. Lindsay, B. Huang, Unusual enhancement in intrinsic thermal conductivity of multilayer graphene by tensile strains, *Nano Lett.* 15 (2015) 6121–6127.
- [51] L. Lindsay, W. Li, N. Mingo, D.A. Broido, J. Carrete, T.L. Reinecke, Phonon thermal transport in strained and unstrained graphene from first principles, *Phys. Rev. B* 89 (2014).
- [52] T. Zhu, E. Ertekin, Resolving anomalous strain effects on two-dimensional phonon flows: the cases of graphene, boron nitride, and planar superlattices, *Phys. Rev. B* 91 (2015).
- [53] X. Li, K. Maute, M.L. Dunn, R. Yang, Strain effects on the thermal conductivity of nanostructures, *Phys. Rev. B* 81 (2010) 245318.
- [54] S. Bagherifard, R. Ghelichi, M. Guagliano, Numerical and experimental analysis of surface roughness generated by shot peening, *Appl. Surf. Sci.* 258 (2012) 6831–6840.
- [55] C. Shao, X. Yu, N. Yang, Y. Yue, H. Bao, A review of thermal transport in low-dimensional materials under external perturbation: effect of strain, substrate, and clustering, *Nanoscale Microsc. Therm.* 21 (2017) 201–236.
- [56] S. Alaie, D.F. Goettler, M. Su, Z.C. Leseman, C.M. Reinke, I. El-Kady, Thermal transport in phononic crystals and the observation of coherent phonon scattering at room temperature, *Nat. Commun.* 6 (2015) 7228.
- [57] S. Chen, Q. Li, Q. Zhang, Y. Qu, H. Ji, R. Ruoff, W. Cai, Thermal conductivity measurements of suspended graphene with and without wrinkles by micro-Raman mapping, *Nanotechnology* 23 (2012) 365701–365701.
- [58] C. Wang, Y. Liu, L. Li, H. Tan, Anisotropic thermal conductivity of graphene wrinkles, *Nanoscale* 6 (2014) 5703–5707.
- [59] J. Guo, X. Wang, T. Wang, Thermal characterization of microscale conductive and nonconductive wires using transient electrothermal technique, *J. Appl. Phys.* 101 (2007) 063537.
- [60] J. Liu, Z. Xu, Z. Cheng, S. Xu, X. Wang, Thermal conductivity of ultrahigh molecular weight polyethylene crystal: defect effect uncovered by 0 K limit phonon diffusion, *ACS Appl. Mater. Inter.* 7 (2015) 27279–27288.
- [61] Y. Xie, P. Yuan, T. Wang, N. Hashemi, X. Wang, Switch on the high thermal conductivity of graphene paper, *Nanoscale* 8 (2016) 17581–17597.
- [62] Z. Xu, X. Wang, H. Xie, Promoted electron transport and sustained phonon transport by DNA down to 10 K, *Polymer* 55 (2014) 6373–6380.
- [63] Y. Xie, Z. Xu, S. Xu, Z. Cheng, N. Hashemi, C. Deng, X. Wang, The defect level and ideal thermal conductivity of graphene uncovered by residual thermal reffusivity at the 0 K limit, *Nanoscale* 7 (2015) 10101–10110.
- [64] C. Deng, Y. Sun, L. Pan, T. Wang, Y. Xie, J. Liu, B. Zhu, X. Wang, Thermal diffusivity of a single carbon nanocoil: uncovering the correlation with temperature and domain size, *ACS Nano* 10 (2016) 9710–9719.
- [65] K. Vanmeensel, A. Lapev, J. Hennicke, J. Vleugels, O. Van der Biest, Modelling of the temperature distribution during field assisted sintering, *Acta Mater.* 53 (2005) 4379–4388.
- [66] M. Hu, J. He, Z. Zhao, T.A. Strobel, W. Hu, D. Yu, H. Sun, L. Liu, Z. Li, M. Ma, Compressed glassy carbon: an ultrastrong and elastic interpenetrating graphene network, *Sci. Adv.* 3 (2017) e1603213.
- [67] A. Alofi, G. Srivastava, Thermal conductivity of graphene and graphite, *Phys. Rev. B* 87 (2013) 115421.
- [68] F. Ma, H.B. Zheng, Y.J. Sun, D. Yang, K.W. Xu, P. Chu, Strain effect on lattice vibration, heat capacity, and thermal conductivity of graphene, *Appl. Phys. Lett.* 101 (2012) 111904.
- [69] Z. Luo, H. Cho, X. Luo, K.i. Cho, System thermal analysis for mobile phone, *Appl. Therm. Eng.* 28 (2008) 1889–1895.
- [70] S.P. Gurrum, D.R. Edwards, T. MarchandGolder, J. Akiyama, S. Yokoya, J. Drouard, F. Dahan, Generic thermal analysis for phone and tablet systems, *Electronic Components and Technology Conference (ECTC), 2012 IEEE 62nd, IEEE, 2012*, pp. 1488–1492.
- [71] S. Azarfar, S. Movahedirad, A. Sarbanha, R. Norouzbegi, B. Beigzadeh, Low cost and new design of transient hot-wire technique for the thermal conductivity measurement of fluids, *Appl. Therm. Eng.* 105 (2016) 142–150.
- [72] T.L. Bergman, F.P. Incropera, D.P. DeWitt, A.S. Lavine, *Fundamentals of Heat and Mass Transfer*, John Wiley & Sons, 2011.
- [73] Y. Li, C. Biber, C. Hengju, Thunderbolt active cable thermal analysis, *Thermal Measurement, Modeling & Management Symposium (SEMI-THERM), 2016*, pp. 206–212.
- [74] J. Ding, O.u. Rahman, H. Zhao, W. Peng, H. Dou, H. Chen, H. Yu, Ultrahigh electrical and thermal conductive hydroxylated graphene based flexible carbon film, *Nanotechnology* 28 (2017).